

Valley photonic crystals for control of spin and topology

Jian-Wen Dong^{1,2†}, Xiao-Dong Chen^{1†}, Hanyu Zhu², Yuan Wang^{2,3} and Xiang Zhang^{2,3,4*}

Photonic crystals offer unprecedented opportunity for light manipulation and applications in optical communication and sensing^{1–4}. Exploration of topology in photonic crystals and metamaterials with non-zero gauge field has inspired a number of intriguing optical phenomena such as one-way transport and Weyl points^{5–10}. Recently, a new degree of freedom, valley, has been demonstrated in two-dimensional materials^{11–15}. Here, we propose a concept of valley photonic crystals with electromagnetic duality symmetry but broken inversion symmetry. We observe photonic valley Hall effect originating from valley-dependent spin-split bulk bands, even in topologically trivial photonic crystals. Valley-spin locking behaviour results in selective net spin flow inside bulk valley photonic crystals. We also show the independent control of valley and topology in a single system that has been long pursued in electronic systems, resulting in topologically-protected flat edge states. Valley photonic crystals not only offer a route towards the observation of non-trivial states, but also open the way for device applications in integrated photonics and information processing using spin-dependent transportation.

Optical degrees of freedom (d.f.), such as frequency, polarization and phase, have been used to modulate the flow of light in complex media, including the accessibility to directional emission and electromagnetic cloaks^{1–4,16,17}. In a metasurface, phase and polarization of light can be altered so as to realize the functionality of ultrathin flat lenses and holograms^{18–21}. By incorporating spin d.f., photonic spin Hall effect and unidirectional transmission were observed^{22–26}. Topological optics has been recently explored in non-trivial systems characterized by photonic forbidden bands with gapless interfacial states^{5–10,27–32}. Such non-trivial topology inspires the fundamental phenomena such as unidirectional transport and Weyl physics, and fault-tolerant photonic devices such as robust delay lines and slow-light optical buffers.

Valley labels the energetically degenerate yet inequivalent points in momentum space. This new d.f. has attracted extensive research in graphene and transition metal dichalcogenides (TMDCs) as an energy-efficient alternative in information technology to charge and spin d.f. In particular, the large direct bandgap and strong spin-orbit coupling in monolayer TMDC enable valley polarization with long lifetime and non-zero Berry phase, producing valley-selective circular dichroism and valley Hall effect^{11–15}. While valley in topological insulators has been theoretically discussed and they have been found to host a quantum valley Hall phase that allows logic devices with ultralow power consumption, it is very challenging to realize it in electronic systems^{33–35}.

Here, we propose a unique concept of valley photonic crystals (VPCs) with electromagnetic duality symmetry but broken

inversion symmetry. Using valley as a d.f., we demonstrate valley-dependent spin-split bulk bands and the resulting photonic valley Hall effect (PVHE). Valley-selective net spin flow is realized

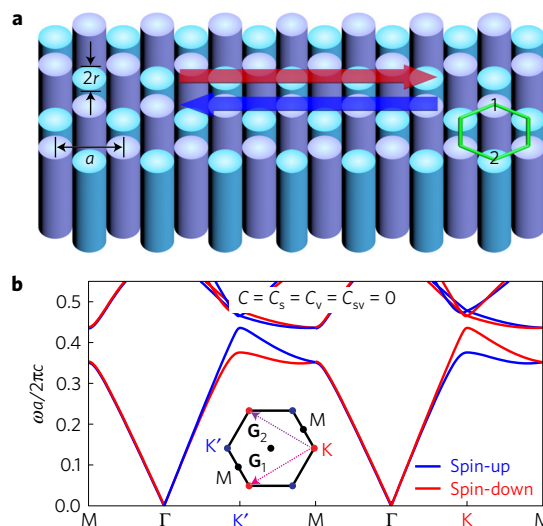


Figure 1 | VPC and valley-dependent spin-split bands. **a**, Schematic of the VPC with electromagnetic duality symmetry but broken inversion symmetry. The electromagnetic duality symmetry is guaranteed by the equivalence between permittivity and permeability. Therefore, the spin can be well defined by the phase difference between the components E_z and H_z , in such a way that the spin-up state is in-phase while the spin-down state is out-of-phase. The inversion asymmetry is achieved by introducing staggered bianisotropic responses with bianisotropic coefficients $\kappa_1 = -0.5$ and $\kappa_2 = 0.5$ for the purple and blue rods, respectively. All the rod radii are set to be $r_1 = r_2 = 0.25a$. The readily realizable metamaterial design is shown in Supplementary Information D. **b**, Valley-dependent spin-split bulk band diagram of spin-up (blue) and spin-down (red) modes. The quadratic bands with spin splitting near the K' and K valleys are consistent with the analysis on the low-energy Hamiltonian $H_0 = \gamma(\delta\mathbf{k})^2 + \lambda\hat{\tau}_z\hat{s}_z$. The non-zero valley-spin coupling term $\lambda\hat{\tau}_z\hat{s}_z$ is derived from the inversion-symmetry-breaking bianisotropic configuration in **a**. Opposite spin splitting is protected by T -symmetry. The spin-down (-up) polarized gap appears from 0.375 to 0.435 (c/a) near the K' (K) valley. In addition, the VPC is topologically trivial as the two lowest monopolar bands are characterized by zero topological invariants. The inset in **b** illustrates the first Brillouin zone of the VPC, and the colours of K' and K are consistent with the arrows in **a**.

¹State Key Laboratory of Optoelectronic Materials and Technologies & School of Physics, Sun Yat-Sen University, Guangzhou 510275, China. ²NSF Nanoscale Science and Engineering Center (NSEC), University of California, Berkeley, California 94720, USA. ³Materials Sciences Division, Lawrence Berkeley National Laboratory, Berkeley, California 94720, USA. ⁴Department of Physics, King Abdulaziz University, Jeddah 21589, Saudi Arabia. [†]These authors contributed equally to this work. *e-mail: xiang@berkeley.edu

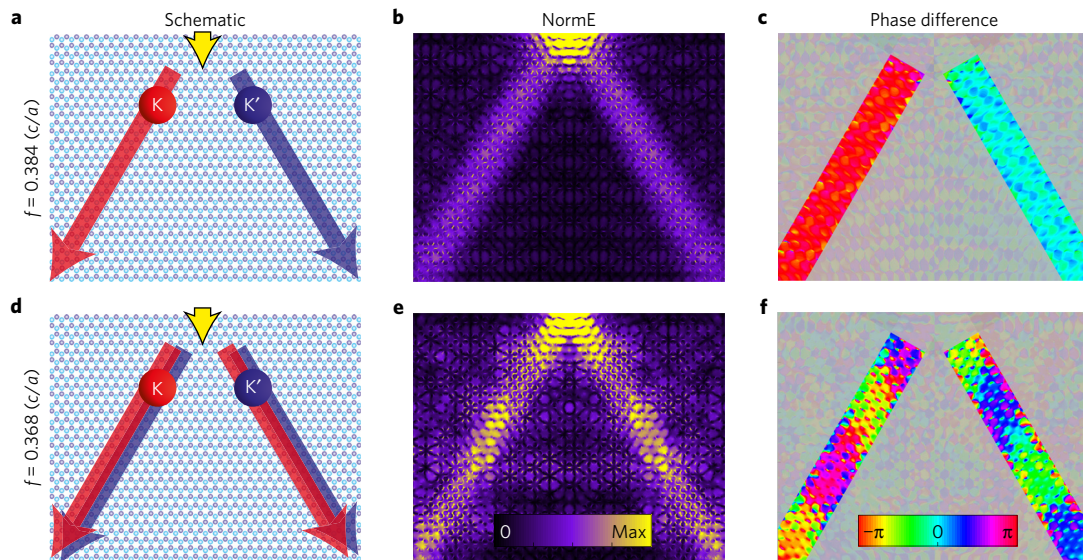


Figure 2 | PVHE in VPC. **a**, Schematic diagram of valley–spin locking. The spin-down (-up) flow can automatically pick out and propagate down-leftwards (-rightwards) along the ΓK ($\Gamma K'$) direction, even when it is excited by the spinless source (yellow arrow) with out-of-plane electric current source and launched from the top to the topologically trivial VPC. The operating frequency is set to be $f = 0.384 (c/a)$ inside the spin gap. **b**, Distributions of the amplitude of electric fields (NormE), showing that the excited wave splits into two beams with uniform patterns along the ΓK and $\Gamma K'$ directions. **c**, Stable phase difference at the value of either π (red) or 0 (blue), indicating that the spin information is well kept inside the VPC as the pure spin mode is excited in either valley. The regions carrying no useful information (low value of NormE) are shaded. **d**, Schematic diagram without PVHE. The simulation setting is the same as in **a** except that the operating frequency changes to be $0.368 (c/a)$ outside the spin gap. Both spin-up and spin-down states are excited and they can propagate downwards along both the ΓK and $\Gamma K'$ directions. **e**, Oscillating pattern of the amplitude of electric fields (NormE) is found due to the interferences between different spin states. **f**, Phase difference between E_z and H_z is messy in both propagating directions, indicating that no spin separation is found.

inside bulk VPCs, in contrast to the spin flow at the boundary of topological photonic crystals. We further show the independent control of valley and topology in a single system, resulting in topologically protected flat edge states. VPCs open up a route towards the discovery of fundamentally novel states of light and applications such as spin-dependent light transport, one-way spin transport, and robust slow light.

We consider a honeycomb VPC with the unit cell of two bianisotropic metamaterial rods separated by vacuum (Fig. 1a). These two rods have radii of $r_1 = r_2 = 0.25a$, where a is the lattice constant, and uniaxial permittivity and permeability $\hat{\epsilon}_r = \hat{\mu}_r = \text{diag}(\epsilon_{11}, \epsilon_{11}, \epsilon_z)$, where $\epsilon_{11} = \epsilon_{21} = 8$ and $\epsilon_{1z} = \epsilon_{2z} = 1$. Throughout the text, the subscripts 1 and 2 refer to rods located at the top and bottom of a hexagonal unit cell, respectively. The bianisotropic coefficient tensor (ζ) for each rod has non-zero elements of $\zeta_{xy} = \zeta_{yx}^* = i\kappa\epsilon_{11}/c$, in which κ describes the magneto-electric coupling strength, and c is the light speed. To break the inversion symmetry, staggered bianisotropic responses, that is, $\kappa_1 = -0.5$ and $\kappa_2 = 0.5$, are applied to the purple and blue rods, respectively. These constitutive parameters of rods are chosen to guarantee the monopolar bulk bands as the lowest bands (Fig. 1b). Due to the electromagnetic duality symmetry, that is, $\hat{\epsilon}_r = \hat{\mu}_r$, the Maxwell equations can be decomposed into two ‘pseudo-spin’ subspaces (‘pseudo-spin’ is abbreviated as ‘spin’ for short throughout the text; see more details in Supplementary Fig. 1b). The dispersions of spin-up and spin-down states are marked with blue and red curves in Fig. 1b, respectively. Bands along the ΓM direction are doubly degenerate protected by mirror symmetry. In contrast, dispersions of different spin states will split in frequency level along other momentum directions owing to valley–spin coupling. The spin splitting is maximum at the valley centre, and it is opposite between the two inequivalent valleys: K' and K due to T -symmetry protection. It leads to a valley-dependent spin gap from 0.375 to 0.435 (c/a). Within the spin gap, when the equi-frequency

contour is perpendicular to the valley momentum (see details in Supplementary Fig. 1d), either the spin-up or spin-down state inside the spin gap will propagate paraxial to the $\Gamma K'$ or ΓK direction, for example, blue or red arrow in Fig. 1a.

To analytically describe the coupled photonic valley–spin physics, we construct a minimal band model of the two lowest monopolar bulk bands. In photonic $\mathbf{k} \cdot \mathbf{p}$ approximation, we can resort to the Hamiltonian (see Supplementary Information A for detailed derivation):

$$H_0 = \gamma(\delta\mathbf{k})^2 + \lambda\hat{\tau}_z\hat{s}_z, \quad (1)$$

where $\delta\mathbf{k}$ is measured from the valley centre K' or K . $\hat{\tau}_z$ and \hat{s}_z are Pauli matrices acting on valley and spin subspaces, respectively. The homogeneous term $\gamma(\delta\mathbf{k})^2$ shows the monopolar nature and controls the band curvatures where $\gamma \propto (\alpha_{G_0} + \alpha_{G_1} + \alpha_{G_2})$ with $\alpha(\mathbf{r}) = 1/[\epsilon_{11}(1 - \kappa^2)]$ and $\alpha(\mathbf{r}) = \sum_G \alpha_G e^{i\mathbf{G}\cdot\mathbf{r}}$. In particular, the valley–spin coupling is reflected by the term $\lambda\hat{\tau}_z\hat{s}_z$, where $\lambda \propto (\theta_{G_1} - \theta_{G_2})$ with $\theta(\mathbf{r}) = \kappa/[\epsilon_{11}(1 - \kappa^2)]$ and $\theta(\mathbf{r}) = \sum_G \theta_G e^{i\mathbf{G}\cdot\mathbf{r}}$. It describes the strength of the coupled valley and spin interaction in which 2λ characterizes the amount of spin splitting at the band top edge. Inferring from the multiplication of $\hat{\tau}_z\hat{s}_z$, valley-dependent spin splitting is expected and verified by numerical simulation (Fig. 1b). Note that the 2λ term will be non-zero if and only if the inversion symmetry is broken by finite bianisotropy, as the spin splitting is determined by the difference between two reciprocal coefficients of θ with inverted vectors. Note also that the above analytical description does not relate to the non-trivial spin–orbit coupling term, meaning that valley d.f. can be exploited even in topologically trivial VPCs. The calculated topological invariants, including the Chern number (C), the spin Chern number (C_s), the valley Chern number (C_v) and the spin valley Chern number (C_{sv}), are equivalent to zero, confirming its trivial topology (Fig. 1b).

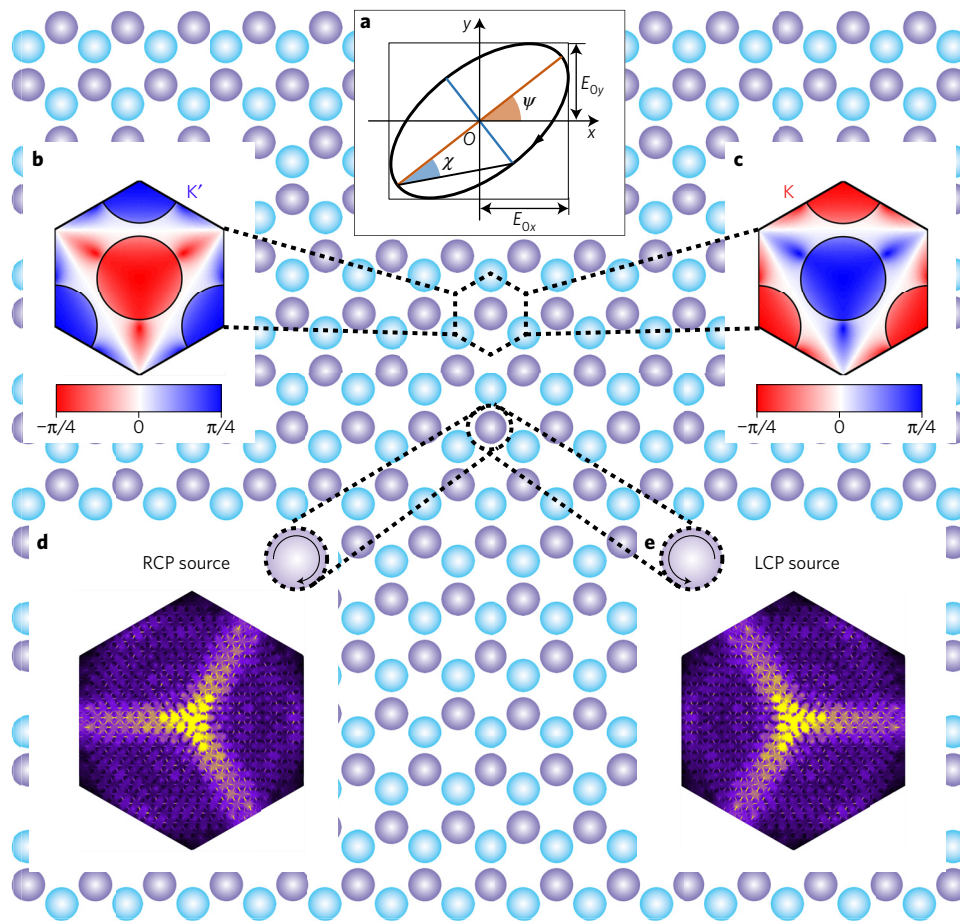


Figure 3 | Valley-dependent polarization and selective net spin flow. **a**, Definition of polarization ellipse. The ellipticity angle ($-\pi/4 \leq \chi \leq \pi/4$) specifies the shape and temporal evolution of the polarization ellipse. In particular, RCP and LCP are characterized by $\chi = \pi/4$ and $\chi = -\pi/4$. **b,c**, Ellipticity angles near the purple rod in real space are shown for the second modes at the K' and K points in Fig. 1b. The interchanged colours in **b** and **c** indicate opposite ellipticity angles for the two modes. This valley-dependent difference is guaranteed by the T -symmetry. In **b**, the purple rod (the central circle in the dashed hexagonal outline) exhibits RCP (red, $\chi = \pi/4$) at K' valley, while in **c**, the purple one shows LCP (blue, $\chi = -\pi/4$) at the K valley. The other characteristics of polarization singularity refer to Supplementary Information C. **d,e**, Selective excitation of the net spin flow inside the VPC. The flow direction depends on the circular polarization of the sources. **d**, Spin-up flow along the $\Gamma K'$ direction is excited by a rotating RCP source at the purple rod, with the working frequency of $0.384 (c/a)$ in the spin gap. **e**, Spin-down flow along the ΓK direction by LCP excitation.

One of the significant manifestations of spin-split behaviours is the valley-controlled spin flow in bulk crystal, for example, PVHE. Here we consider a spinless E_z source launching from the top (Fig. 2a). When the operating frequency is $0.384 (c/a)$ inside the spin gap, due to the photonic valley–spin coupling in the VPC, the spin-down component from the source can be filtered out and routed down-leftwards along the ΓK direction, while the spin-up component is transferred along the $\Gamma K'$ direction. This valley-dependent spin-flow behaviour is well demonstrated as the electric intensity patterns are nearly uniform along both the ΓK and $\Gamma K'$ directions (Fig. 2b). Another feature in PVHE is spin-maintainability in different valleys. This is verified in Fig. 2c, which shows that the phase difference between E_z and H_z is stable around the value of π (red), indicating the nearly pure spin-down state along the ΓK direction. On the contrary, the propagating spin-up wave along the $\Gamma K'$ direction has the phase difference of near zero (blue). Similar spin-maintainable behaviours will occur for higher frequency (Supplementary Information B and Supplementary Fig. 2). As a comparison, we also study the wave propagation without spin separation at the frequency of $0.368 (c/a)$ outside the spin gap (Fig. 2d–f). Both spin-up and spin-down states are excited, and the interferences of the two spin states result in the field oscillations (Fig. 2e) and the messy

phase difference distributions (Fig. 2f). Thus, no pure spin flow is found. Therefore, PVHE is confirmed within the spin gap in such a way that spin flow from the two inequivalent valleys can route to different directions.

It should be noted that the K' and K valleys are correlated by T -symmetry and thus for a mode at the K' valley with an in-plane rotating polarization, the time-reversal counter-propagating mode at the K valley has the orthogonal rotating polarization. As a result, the valley-dependent polarization is expected. To elaborate this, we define the ellipticity angle χ ($-\pi/4 \leq \chi \leq \pi/4$, Fig. 3a), which specifies the shape and temporal evolution of the polarization ellipse³⁶. On the other hand, the orientation angle ($0 \leq \psi < \pi$) determines the angle between the major axis and the coordinate axis Ox (Supplementary Information C). Figure 3b,c shows the ellipticity angles of the second lowest modes at the K' and K points near the purple rod in real space. The valley-dependent polarization is inferred from the interchanged colours between Fig. 3b,c, as the colour of red (blue) represents clockwise (anticlockwise) rotating polarization. Specifically, right-handed circular polarization (RCP) and left-handed circular polarization (LCP) characterized by $\chi = \pi/4$ and $\chi = -\pi/4$ exist in the centre of the purple rods for the modes at the K' and K points, respectively. The valley-dependent polarization gives the possibility to select the output channel of the

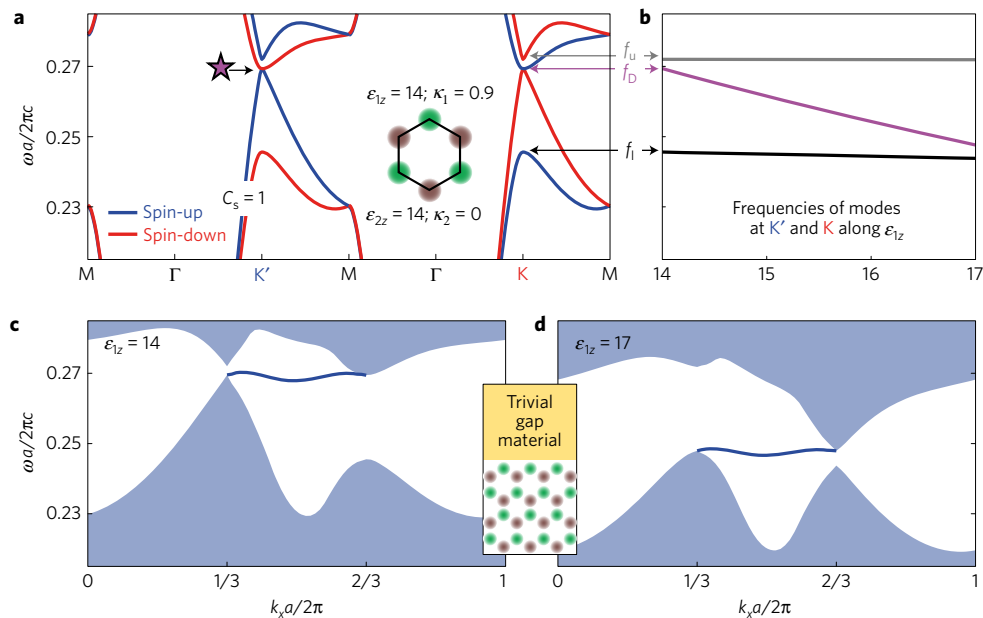


Figure 4 | Independent control of valley and topology in a photonic crystal with the bianisotropy-nonbianisotropy configuration. **a**, Valley-dependent spin-up (blue) and spin-down (red) band diagram. Inset: the crystalline unit cell consists of two sets of rods with the radius of $0.2a$ and the constitutive parameters of $\hat{\epsilon}_r = \hat{\mu}_r = \text{diag}(1, 1, 14)$. The bianisotropic term $\kappa_1 = 0.9$ is for the green rod while the brown one has zero bianisotropy. The topology is non-trivial as the calculated spin Chern number is $C_s = 1$, determined by the large spin-orbit coupling. The star marks the hetero-spin degenerate point at which the two different-spin bulk bands are structurally degenerate. The realistic design is shown in Supplementary Information D. **b**, Evolution of frequencies for the modes at the valley centre as a function of the z -component permittivity of the green rod, ϵ_{1z} , illustrating the tunability of the hetero-spin degenerate mode and the flat edge state. **c,d**, Flat edge dispersions in a photonic crystal with $\epsilon_{1z} = 14$ (**c**) and $\epsilon_{1z} = 17$ (**d**). Only the spin-up polarized projection bands (shaded blue region) and the spin-up edge states are illustrated, as those for the spin-down polarization simply obey $\omega^\downarrow(\mathbf{k}) = \omega^\uparrow(-\mathbf{k})$. The interface constructed by capping the VPC with a trivial gap material on the top is schematically shown in the middle inset.

spin flow in bulk crystal. This is verified when a rotating in-plane electric dipolar source with different circular polarization is placed at the purple rod, with the frequency of $0.384 (c/a)$ inside the spin gap. When the in-plane source is clockwise RCP, the spin-up bulk states within the K' valley will be coupled, and thus the wave is just confined along the three $\Gamma K'$ directions, exhibiting the C_3 rotational symmetry (Fig. 3d). If the source changes to be anticlockwise LCP, the spin-down state is selected to excite and the wave propagating direction is reversed (Fig. 3e).

It is challenging to independently control both valley and topology in a single system, while the proposed VPC is a potential platform to solve the issue. We alter the radii of the two rods to be $0.2a$ and the constitutive parameters to be $\hat{\epsilon}_r = \hat{\mu}_r = \text{diag}(1, 1, 14)$. Such modified configurations lead to the symmetry of the lowest bulk band varying from monopolarity to conical type (see Supplementary Fig. 8 and SE for detailed band evolution). The conical band is dipolar and introduces an additional orbit d.f. It enables the control of topology through the non-trivial photonic spin-orbit coupling that is approximately provided by the net bianisotropy ($\kappa_1 + \kappa_2$). Note that the valley-spin coupling is intrinsic in the VPC, and it is approximately determined by the staggered bianisotropy ($\kappa_1 - \kappa_2$). Consequently, the independent control of valley and topology can be achieved in such a conical-type VPC.

To achieve a new topological phase, we consider the VPC with the bianisotropy-nonbianisotropy configuration such that the green rod (inset of Fig. 4a) is set to be bianisotropic ($\kappa_1 = 0.9$) while keeping the brown one to be nonbianisotropic ($\kappa_2 = 0$). This configuration will lead to the non-zero valley-spin coupling induced by inversion asymmetric bianisotropy. As stated above, the valley-dependent spin-split bands will be present, confirmed in the separated blue and red bands in Fig. 4a. Therefore, the valley-controlled behaviours such as PVHE and selective net spin flow can be expected. In addition, in contrast to the staggered bianisotropic arrangement

in the trivial VPC in Fig. 1, the VPC with the bianisotropy-nonbianisotropy configuration is topologically non-trivial as the spin-orbit coupling is obviously non-zero. This is verified by the non-zero Chern numbers of the lowest spin-up and spin-down bands, that is, $C^\uparrow = 1$, $C^\downarrow = -1$ and $C_s = 1$, calculated by the group theory method²⁹. We would like to emphasize that the VPC in Fig. 4a is topologically distinct from most of the monolayer TMDC.

An interesting issue is that the bianisotropy-nonbianisotropy configuration guarantees the balance of the non-zero valley-spin coupling and non-zero spin-orbit coupling in a single system. It enables one to construct the peculiar dispersion such that the two different-spin bulk bands are structurally degenerate at the valley centre, so-called hetero-spin degeneracy (star in Fig. 4a). This degeneracy is constructed by two modes with the same orbital index but different spin indices, and is structurally protected due to the same strengths between photonic valley-spin coupling and spin-orbit coupling. It brings a new opportunity to realize valley-related flat edge states protected by non-trivial topology. As shown in Fig. 4c, there is a gapless flat spin-up state at the hetero-spin degenerate frequency of $f_D = 0.27 (c/a)$, connecting from the lower band at the K' valley to the upper band at the K valley, at the edge between the non-trivial VPC and a trivial bandgap material. Such a flat edge state is tunable by the constitutive parameters of the rod. For example, Fig. 4b plots that the hetero-spin degenerate frequency f_D decreases monotonically when ϵ_{1z} increases from 14 to 17, while the frequencies of the upper and lower modes (f_u and f_l) change a little. Thus, the flat edge dispersion will shift to a lower frequency for larger ϵ_{1z} , confirmed by Fig. 4d, where $\epsilon_{1z} = 17$. Note that these flat edge states are not robust against defects, as the number difference is zero between the positive and negative group velocity edge modes.

To conclude, we propose a concept of VPC with valley d.f. This class of photonic crystal has electromagnetic duality symmetry but broken inversion symmetry. The valley-dependent spin-split

bulk bands allow us to observe the PVHE and selective net spin flow inside the bulk crystals. In addition, these valley-contrasting phenomena are achieved even in the trivial VPCs, indicating that non-trivial topology is not necessary for the manipulation of spin flow. We further realize the independent control of valley and topology in a single system, which has been long pursued in electronic materials. For the experimental implementation of the proposed VPCs in Figs 1b and 4a, the realistic metamaterial designs are outlined in Supplementary Information D. Both the bulk band structures and the eigen-field patterns for the experimental designs show good agreement with the theoretical results.

We would like to emphasize that similar valley-dependent behaviours can also be exploited by breaking inversion symmetry in other photonic systems such as three-dimensional photonic crystals, silicon photonics, and gyrotropic medium. VPCs provide a gateway to fundamental physics that is difficult to observe in electronic systems, but could also be relevant for the implementation of optical communication devices based on spin-dependent transport and robust flow of light, and spin-orbital angular momentum of light.

Methods

Methods and any associated references are available in the [online version of the paper](#).

Received 18 February 2016; accepted 26 October 2016;
published online 28 November 2016

References

- Yablonovitch, E. Inhibited spontaneous emission in solid-state physics and electronics. *Phys. Rev. Lett.* **58**, 2059–2062 (1987).
- John, S. Strong localization of photons in certain disordered dielectric superlattices. *Phys. Rev. Lett.* **58**, 2486–2489 (1987).
- Joannopoulos, J. D., Villeneuve, P. R. & Fan, S. Photonic crystals: putting a new twist on light. *Nature* **386**, 143–149 (1997).
- Huang, X., Lai, Y., Hang, Z. H., Zheng, H. H. & Chan, C. T. Dirac cones induced by accidental degeneracy in photonic crystals and zero-refractive-index materials. *Nat. Mater.* **10**, 582–586 (2011).
- Wang, Z., Chong, Y. D., Joannopoulos, J. D. & Soljačić, M. Observation of unidirectional backscattering-immune topological electromagnetic states. *Nature* **461**, 772–775 (2009).
- Lu, L., Joannopoulos, J. D. & Soljačić, M. Topological photonics. *Nat. Photon.* **8**, 821–829 (2014).
- Khanikaev, A. B. *et al.* Photonic topological insulators. *Nat. Mater.* **12**, 233–239 (2013).
- Hafezi, M., Demler, E. A., Lukin, M. D. & Taylor, J. M. Robust optical delay lines with topological protection. *Nat. Phys.* **7**, 907–912 (2011).
- Rechtsman, M. C. *et al.* Photonic Floquet topological insulators. *Nature* **496**, 196–200 (2013).
- Lu, L., Fu, L., Joannopoulos, J. D. & Soljačić, M. Weyl points and line nodes in gyroid photonic crystals. *Nat. Photon.* **7**, 294–299 (2013).
- Xiao, D., Yao, W. & Niu, Q. Valley-contrasting physics in graphene: magnetic moment and topological transport. *Phys. Rev. Lett.* **99**, 236809 (2007).
- Xu, X., Yao, W., Xiao, D. & Heinz, T. F. Spin and pseudospins in layered transition metal dichalcogenides. *Nat. Phys.* **10**, 343–350 (2014).
- Mak, K. F., McGill, K. L., Park, J. & McEuen, P. L. The valley Hall effect in MoS₂ transistors. *Science* **344**, 1489–1492 (2014).
- Ye, Z. *et al.* Probing excitonic dark states in single-layer tungsten disulphide. *Nature* **513**, 214–218 (2014).
- Ye, Y. *et al.* Monolayer excitonic laser. *Nat. Photon.* **9**, 733–737 (2015).
- Pendry, J. B., Holden, A. J., Stewart, W. J. & Youngs, I. Extremely low frequency plasmons in metallic mesostructures. *Phys. Rev. Lett.* **76**, 4773–4776 (1996).
- Smith, D. R., Padilla, W. J., Vier, D. C., Nemat-Nasser, S. C. & Schultz, S. Composite medium with simultaneously negative permeability and permittivity. *Phys. Rev. Lett.* **84**, 4184–4187 (2000).
- Yu, N. & Capasso, F. Flat optics with designer metasurfaces. *Nat. Mater.* **13**, 139–150 (2014).
- Ni, X., Kildishev, A. V. & Shalaev, V. M. Metasurface holograms for visible light. *Nat. Commun.* **4**, 2807 (2013).
- Yin, X., Ye, Z., Rho, J., Wang, Y. & Zhang, X. Photonic spin Hall effect at metasurfaces. *Science* **339**, 1405–1407 (2013).
- High, A. A. *et al.* Visible-frequency hyperbolic metasurface. *Nature* **552**, 192–196 (2015).
- Bliokh, K. Y., Smirnova, D. & Nori, F. Quantum spin Hall effect of light. *Science* **348**, 1448–1451 (2015).
- Lin, J. *et al.* Polarization-controlled tunable directional coupling of surface plasmon polaritons. *Science* **340**, 331–334 (2013).
- Petersen, J., Volz, J. & Rauschenbeutel, A. Chiral nanophotonic waveguide interface based on spin-orbit interaction of light. *Science* **346**, 67–71 (2014).
- Young, A. B. *et al.* Polarization engineering in photonic crystal waveguides for spin-photon entanglers. *Phys. Rev. Lett.* **115**, 153901 (2015).
- Söllner, I. *et al.* Deterministic photon-emitter coupling in chiral photonic circuits. *Nat. Nano.* **10**, 775–778 (2015).
- Fang, K., Yu, Z. & Fan, S. Realizing effective magnetic field for photons by controlling the phase of dynamic modulation. *Nat. Photon.* **6**, 782–787 (2012).
- Chen, W. J. *et al.* Experimental realization of photonic topological insulator in a uniaxial crystal waveguide. *Nat. Commun.* **5**, 5782 (2014).
- Chen, X. D., Deng, Z. L., Chen, W. J., Wang, J. R. & Dong, J. W. Manipulating pseudospin-polarized state of light in dispersion-immune photonic topological metacrystals. *Phys. Rev. B* **92**, 014210 (2015).
- Ma, T. & Shvets, G. All-Si valley-Hall photonic topological insulator. *New J. Phys.* **18**, 025012 (2016).
- Gao, W. *et al.* Topological photonic phase in chiral hyperbolic metamaterials. *Phys. Rev. Lett.* **114**, 037402 (2015).
- Xiao, M., Chen, W.-J., He, W.-Y. & Chan, C. T. Synthetic gauge flux and Weyl points in acoustic systems. *Nat. Phys.* **11**, 920–924 (2015).
- Qiao, Z., Tse, W.-K., Jiang, H., Yao, Y. & Niu, Q. Two-dimensional topological insulator state and topological phase transition in bilayer graphene. *Phys. Rev. Lett.* **107**, 256801 (2011).
- Lensky, Y. D., Song, J. C. W., Samutpraphoot, P. & Levitov, L. S. Topological valley currents in gapped Dirac materials. *Phys. Rev. Lett.* **114**, 256601 (2015).
- Tahir, M. & Schwingenschlögl, U. Valley polarized quantum Hall effect and topological insulator phase transitions in silicene. *Sci. Rep.* **3**, 1075 (2013).
- Born, M. & Wolf, E. *Principles of Optics: Electromagnetic Theory of Propagation, Interference and Diffraction of Light* 7th edn (Cambridge Univ. Press, 1999).

Acknowledgements

This work was primarily funded by the 'Light-Material Interactions in Energy Conversion' Energy Frontier Research Center funded by the US Department of Energy, Office of Science, Office of Basic Energy Sciences under Award Number DE-AC02-05CH11231; the analysis of the bianisotropy–nonbianisotropy configuration is supported by the Office of Naval Research (ONR) MURI programme under Grant No. N00014-13-1-0678. J.-W.D. acknowledges support from the Natural Science Foundation of China (11522437, 11274396), the Guangdong Natural Science Funds for Distinguished Young Scholar (S2013050015694), Guangdong special support program, and the SYSU visiting grant.

Author contributions

X.Z. and J.-W.D. conceived the project. J.-W.D. and X.-D.C. developed and completed the idea. J.-W.D., X.-D.C., H.Z. and Y.W. analysed the data. All authors contributed to discussions and manuscript writing.

Additional information

Supplementary information is available in the [online version of the paper](#). Reprints and permissions information is available online at www.nature.com/reprints. Correspondence and requests for materials should be addressed to X.Z.

Competing financial interests

The authors declare no competing financial interests.

Methods

Simulation. The first-principle electromagnetic simulations in the text were performed with COMSOL Multiphysics after adding bianisotropic constitutive equations into the software. Spin classification in Figs 1b and 4a was carried out by inspecting the relation between the electromagnetic components E_z and H_z . See Supplementary Information A for detailed spin classification.

For the PVHE, the simulated photonic crystal has a size of $52a \times 14.5\sqrt{3}a$ and it is terminated with a zigzag boundary in the upper/lower edge and an armchair boundary in the left/right edge. The out-of-plane electric current source with the width of $0.5a$ is set in the middle of the upper edge. The perfect matched layer with the thickness of $3.5a$ is employed to absorb the propagating waves along the ΓK and $\Gamma K'$ directions. In the simulation, there is a little reflected wave caused by the interface between the photonic crystal and the perfect matched layer. This backscattered wave is laterally guided, and lastly leaks out through the scattering boundary on the leftmost and rightmost edges.

To describe the polarization ellipse of the in-plane electric field, we acquire the amplitude ratio, $\beta = \arctan(E_{0y}/E_{0x})$, and the phase difference between E_y and E_x , $\delta = \delta_y - \delta_x$. The ellipticity angles in Fig. 3b,c were obtained by $\sin(2\chi) = \sin(2\beta) \sin(\delta)$ ³⁶. For the selective net spin flow shown in Fig. 3d,e, the

photonic crystal has a hexagonal shape with the side length of $20.5a/\sqrt{3}$ and it is terminated with armchair boundaries. Two cross-polarized in-plane electric dipoles, one along the y direction and the other along the x direction, are placed at the centre of the purple rod and serve as the source of circular polarization. Their amplitudes are kept the same while the phase difference in between is set to be $\pi/2$ or $-\pi/2$ to mimic the clockwise RCP or anti-clockwise LCP source. One possible experimental scheme of the rotating sources is to apply quantum dots with circularly polarized transition dipoles²⁶.

The edge dispersions shown in Fig. 4c,d were performed by a supercell with the size of $a \times 20\sqrt{3}a$. The height of the supercell is set to ensure minimal coupling between modes at the parallel edges. The distance between the capping trivial gap material and the VPC was set to be $0.25a$. For simplicity, the gap material was set to be homogeneous with anisotropic constitutive parameters of $\hat{\epsilon}_r = \hat{\mu}_r = \text{diag}(1, 1, -10,000)$ and zero bianisotropy, in which both spin states are gapped. One can replace such artificial gap material with another trivial photonic crystal, and topologically non-trivial edge states do still exist.

Code availability. The codes that support the plots within this paper are available from the corresponding author on request.